JGR Solid Earth

RESEARCH ARTICLE
10.1029/2022JB024805

Special Section:
Heterogeneity, anisotropy and scale-dependency: Keys to understand Earth composition, structure and behavior

Age-Independent Oceanic Plate Thickness and Asthenosphere Melting From *SS* Precursor Imaging

Shuyang Sun[1] and **Ying Zhou**[1]

[1]Department of Geosciences, Virginia Tech, Blacksburg, VA, USA

Abstract The Earth's asthenosphere is a mechanically weak layer characterized by low seismic velocity and high attenuation. The nature of this layer has been strongly debated. In this study, we process 12 years of seismic data recorded at the global seismological network stations to investigate *SS* waves reflected at the upper and lower boundaries of this layer in global oceanic regions. We observe strong reflections from both the top and the bottom of the asthenosphere, dispersive across all major oceans. The average depths of the two discontinuities are 120 and 255 km, respectively. The *SS* waves reflected at the lithosphere and asthenosphere boundary are characterized by anomalously large amplitudes, which require a ~12.5% reduction in seismic velocity across the interface. This large velocity drop can not be explained by a thermal cooling model but indicates 1.5%–2% localized melt in the oceanic asthenosphere. The depths of the two discontinuities show large variations, indicating that the asthenosphere is far from a homogeneous layer but likely associated with strong and heterogeneous small-scale convection in the oceanic mantle. The average depths of the two boundaries are largely constant across different age bands. In contrast to the half-space cooling model, this observation supports the existence of a constant-thickness plate in oceanic regions with a complex and heterogeneous origin.

Plain Language Summary In the plate tectonic theory, the outermost shell of the Earth consists of a small number of rigid plates (lithosphere) moving horizontally on the mechanically weak asthenosphere. In oceanic regions, the lithosphere is thought to be formed by the gradual cooling of the hot mantle. Therefore, the thickness of the plate depends on the age of the seafloor. The problem with the classic half-space cooling model is that bathymetry and heat flow measurements at old seafloors do not follow its predicted age dependence. A modified theory, called the plate model, can better explain those geophysical observations by assuming additional heat at the base of an oceanic plate with a constant thickness of about 125 km. However, such a constant-thickness plate has not been observed in seismology. In this study, we image the asthenosphere boundaries using a global dataset of seismic waves reflected off the Earth's internal boundaries. We observe strong reflections from both the top and the bottom of the asthenosphere, across all major oceans. The amplitudes of these waves can be explained by 1.5%–2% of partial melt and the average boundary depths are independent of seafloor age. This observation supports the existence of a constant-thickness plate in the global oceans with a complex origin.

Key Points:

- *SS* precursors reveal depths of the lithosphere–asthenosphere boundary independent of seafloor age
- The oceanic lithosphere–asthenosphere boundary is a strong reflector and can be explained by 1.5%–2% of partial melt
- Large depth variations of the top and the bottom boundaries of the asthenosphere suggest a heterogeneous melting process

Supporting Information:

Supporting Information may be found in the online version of this article.

Correspondence to:

S. Sun,
sysun@vt.edu

Citation:

Sun, S., & Zhou, Y. (2023). Age-independent oceanic plate thickness and asthenosphere melting from *SS* precursor imaging. *Journal of Geophysical Research: Solid Earth*, *128*, e2022JB024805. https://doi.org/10.1029/2022JB024805

Received 18 MAY 2022
Accepted 23 JAN 2023

Author Contributions:

Conceptualization: Shuyang Sun, Ying Zhou
Data curation: Shuyang Sun, Ying Zhou
Formal analysis: Shuyang Sun, Ying Zhou
Funding acquisition: Ying Zhou
Investigation: Shuyang Sun, Ying Zhou
Methodology: Shuyang Sun, Ying Zhou

1. Introduction

In the plate tectonic theory, the outermost shell of the Earth consists of a small number of rigid plates (lithosphere) moving horizontally on the mechanically weak asthenosphere. The origin of the asthenosphere as well as the defining mechanism of its top and bottom rheological interfaces have been highly controversial (Fischer et al., 2010, 2020; Gaherty & Jordan, 1995; Karato, 1992; Kawakatsu & Utada, 2017; Rychert et al., 2012, 2020). The oceanic plates make up ~70% of the Earth's surface and they have a relatively simple geological and tectonic history, therefore they are ideal for resolving these fundamental questions. The classic half-space cooling model predicts that the thickness of the thermal boundary layer as well as the depth of the ocean increase proportionally with the square root of the sea-floor age. While this simple conductive cooling model successfully explains the first-order observations in the oceans, bathymetry and heat flow measurements at seafloor older than ~70 million years do not follow the age dependence predicted by the half space cooling model. The plate model, which assumes additional heat at the base of an oceanic plate with a constant thickness, successfully explains the flattening of sea floor depth and heat flow observations (Parsons & Sclater, 1977). However, such a constant-thickness plate has not been observed in seismology, and the exact source of the additional heat remains unclear, probably

Project Administration: Ying Zhou
Resources: Shuyang Sun, Ying Zhou
Software: Shuyang Sun, Ying Zhou
Supervision: Ying Zhou
Validation: Shuyang Sun, Ying Zhou
Visualization: Shuyang Sun
Writing – original draft: Shuyang Sun
Writing – review & editing: Ying Zhou

associated with small-scale convections (Parsons & Sclater, 1977; Richards et al., 2020; Richter, 1973; Richter & Parsons, 1975) or oceanic hotspots (Korenaga & Korenaga, 2008).

It is a general feature in global seismic surface wave studies that the high-velocity lid in oceanic regions becomes thicker with sea-floor age (French et al., 2013; Godfrey et al., 2017; James et al., 2014; Ma & Dalton, 2019). It has also been suggested that a plate model with additional heat at a constant depth of about 125 km fits surface wave observations (Maggi et al., 2006). Recent surface-wave studies suggest a small amount of melt is trapped within the entire low-velocity oceanic asthenosphere (Debayle et al., 2020), which might provide the additional heat required by the plate model. The depths of the lithosphere–asthenosphere boundary (LAB hereinafter) have also been studied using secondary seismic phases reflected or converted at the interface, including *SS* precursors (Rychert & Shearer, 2011; Schmerr, 2012; Tharimena et al., 2017), receiver functions (Kawakatsu et al., 2009; Li et al., 2000, 2004; Rychert & Shearer, 2009) and active source studies (Mehouachi & Singh, 2018; Stern et al., 2015). Those studies suggest large variations as well as an origin of the asthenosphere much more complex than gradual thermal variations with depth as predicted in the half space cooling model (D. Turcotte & Oxburgh, 1967). A variety of rheological mechanisms have been proposed, including a change in grain size (Faul & Jackson, 2005), seismic anisotropy (Auer et al., 2015; Beghein et al., 2014; Karato & Wu, 1993), elastically accommodated grain boundary sliding (Karato, 2012), and near melting (Yamauchi & Takei, 2016). The large velocity drop and high attenuation also make partial melt a dominant mechanism in many studies (Debayle et al., 2020; Fischer et al., 2020; Kawakatsu et al., 2009; Li et al., 2000, 2004; Mehouachi & Singh, 2018; Rychert et al., 2020; Schmerr, 2012; Stern et al., 2015; Tharimena et al., 2017). For example, a thin sublithosphere melt channel beneath the normal oceanic seafloor has been proposed for the equatorial Atlantic Ocean (Mehouachi & Singh, 2018).

The velocity increase at the base of the asthenosphere has been incorporated in the widely used 1-D global reference earth model, PREM, with about ∼7% of velocity increase across the 220-km discontinuity (Dziewonski & Anderson, 1981). A discontinuity at about this depth was first observed in Europe and North America (Hales et al., 1980; Lehmann, 1959, 1961) and later confirmed by studies using surface-wave dispersion measurements, underside seismic reflections, ScS reverberations, and receiver functions (Goncz & Cleary, 1976; Revenaugh & Jordan, 1991; Sacks et al., 1979; Vidale & Benz, 1992). This discontinuity has been reported in continental regions and is also called the Lehmann discontinuity. However, many studies have concluded that the 220-km discontinuity is not global in nature and a reflection from this depth is missing in the global long-period stacks (Deuss & Woodhouse, 2002, 2004; Gu et al., 2001; Schmerr & Garnero, 2006; Shearer, 1991), which indicates that the existence of the discontinuity is either absent in oceanic regions, or there are large variations in the depth of this discontinuity.

In this study, we analyze 12 years of long-period transverse component seismograms recorded at 151 GSN stations (Figure S1 of Supporting Information S1) to investigate *SS* waves reflected at the top and the bottom of the asthenosphere in oceanic regions, namely, the $S_{LAB}S$ wave reflected at the LAB and the $S_{220}S$ reflected at the bottom of the asthenosphere. We will interpret the low velocity zone (LVZ) between the two discontinuities observed in oceanic regions as the asthenosphere ("weak layer") as it roughly corresponds to the depth range of the global LVZ in model PREM. This is the depth range where geotherm may exceed mantle solidus and partial melt occurs (D. L. Turcotte & Schubert, 2002).

2. Data and Methods

SS precursors are underside reflections from internal discontinuities and they arrive before the main *SS* waves which are reflected at the surface of the Earth. *SS* precursors are very sensitive to the structures of the interfaces at the reflection midpoints, about halfway between the earthquake and the station. They provide good data coverage in the global oceanic areas where seismic stations are sparse. In this study, we examine 32,369 broadband seismograms at 151 GSN stations from 543 earthquakes that occurred between January 2009 and December 2020 with *SS*-wave reflection points in oceanic regions (Figures 1 and 2). The moment magnitude of the earthquakes ranges from 6.0 to 8.0 such that *SS* precursors are excited by potentially sufficient seismic energy (Schmerr, 2012). We download seismograms from the Data Management Center at the Incorporated Research Institutions for Seismology (IRIS). The instrument responses are removed and the East–West and North–South component displacement seismograms are rotated to obtain the radial and transverse component seismograms.

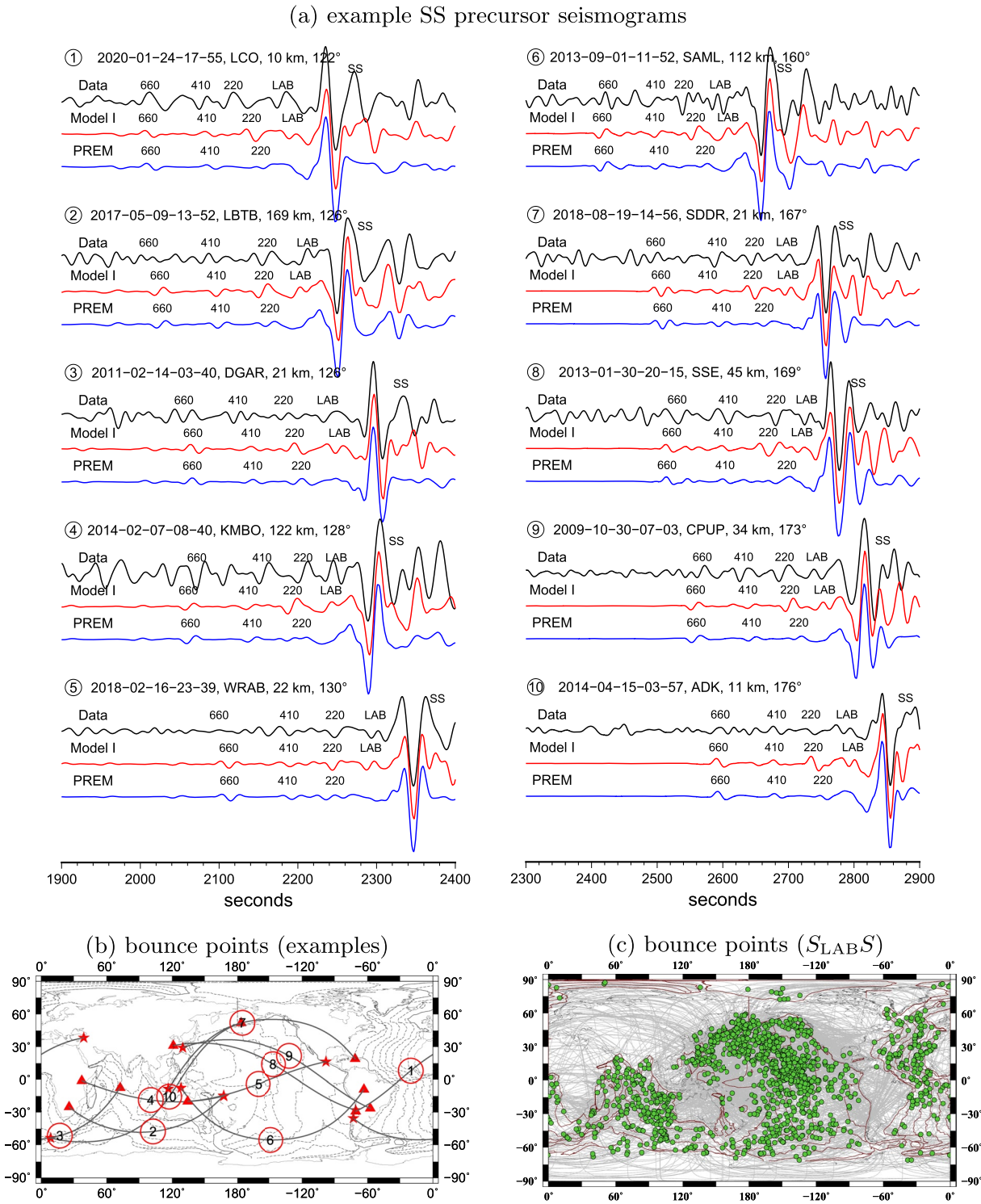

Figure 1. (a) Example transverse-component seismograms with large-amplitude $S_{LAB}S$ and $S_{220}S$ phases. The black seismograms are data, the red seismograms are synthetics calculated in a reference 1-D model (Model I) with 12.5% of the velocity jump across the lithenosphere–asthenosphere boundary (LAB), and the blue synthetics are calculated in PREM in which there is no discontinuity at the LAB depth. The reference models are plotted in Figure 3. The seismograms have been band-pass filtered between 10 and 80 mHz and aligned using their *SS* arrivals for better illustration. The precursor closest to the main *SS* wave is labeled as $S_{LAB}S$ as we investigate possible reflections from the top of the asthenosphere. The arrivals of the $S_{220}S$, $S_{410}S$, and $S_{660}S$ waves are also labeled. The earthquake event date/time and station name as well as depth and epicentral distance are denoted on each seismogram. The corresponding geographic ray paths (black lines) and bounce points (red circles) of the $S_{LAB}S$ waves are plotted in (b). Ray paths (gray lines) and bounce points (green dots) of the 1,380 $S_{LAB}S$ waves with anomalously large amplitudes are plotted in (c). Seafloor age contours are plotted at 20, 60, 100, and 140 Ma.

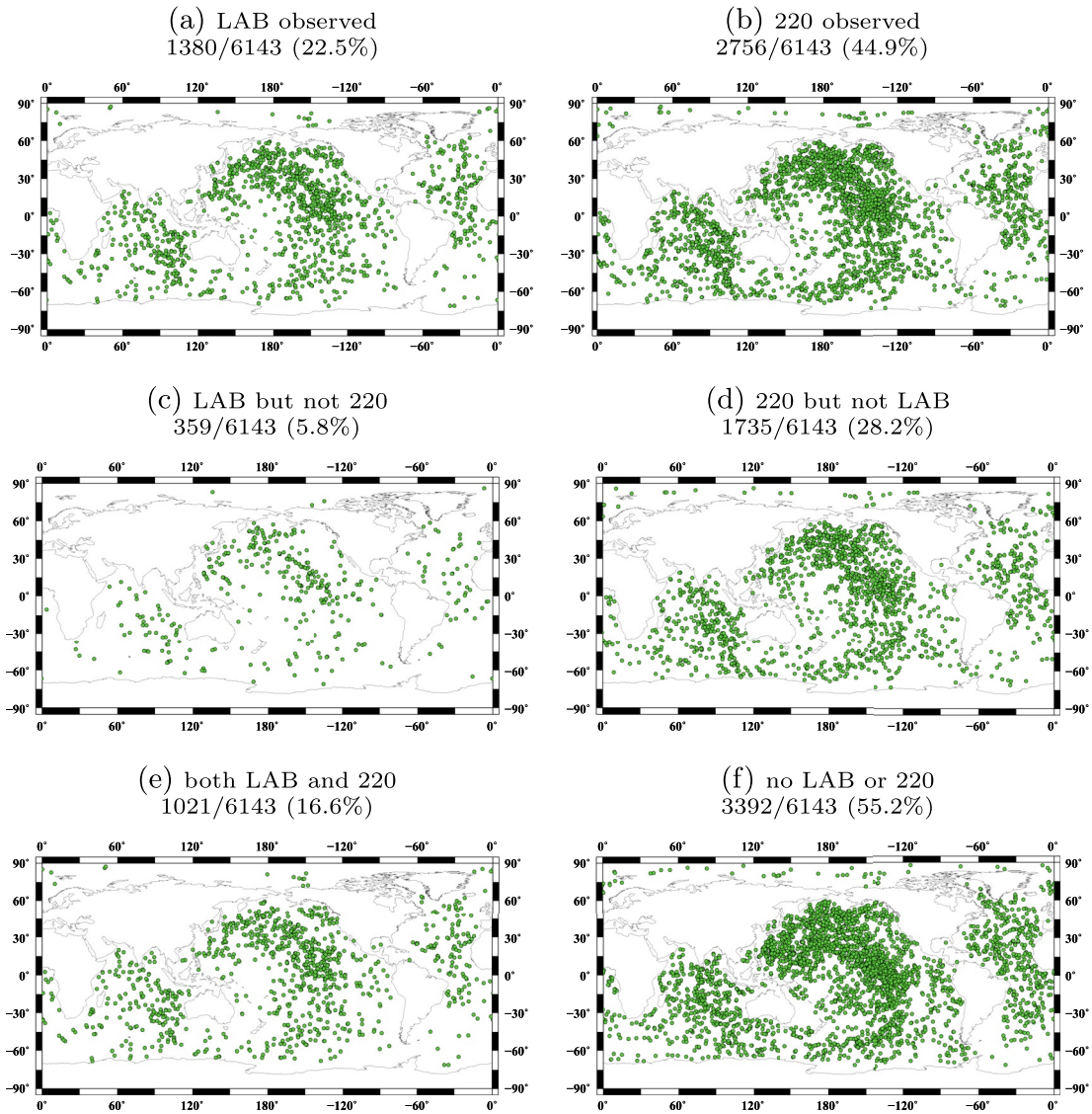

Figure 2. Geographic distribution of subsets of the data plotted at *SS* bounce points. (a) clear $S_{LAB}S$ observed, (b) clear $S_{220}S$ observed, (c) $S_{LAB}S$ observed but not $S_{220}S$, (d) $S_{220}S$ observed but not $S_{LAB}S$, (e) both $S_{LAB}S$ and $S_{220}S$ observed, (f) no $S_{LAB}S$ or $S_{220}S$ observed. There is no apparent geographic pattern associated with either the presence or absence of the $S_{LAB}S$ and $S_{220}S$.

The seismograms are band-pass filtered between 10 and 80 mHz and decimated to 0.1 s sampling interval. Seismograms with weak or complex *SS* waves due to source processes are discarded (Figures S2 and S3 of Supporting Information S1). Seismograms with noisy *SS* waves and precursors are also discarded (Figure S3 of Supporting Information S1). This leaves 6,143 sets of transverse component seismograms with epicentral distances greater than 80°. We visually inspect seismograms for *SS* precursors, including $S_{LAB}S$, $S_{220}S$, $S_{410}S$, and $S_{660}S$. Clear $S_{LAB}S$ arrivals are identified on 1,380 seismograms (about 22.5% of the entire dataset) from 144 stations and 395 earthquakes (Figures 1 and 2). The majority of the data with strong $S_{LAB}S$ waves (981 out of 1,380) have focal depths shallower than 45 km, and the epicentral distance varies between 80.1° and 176.3° with the majority larger than 100° (Figure S1 of Supporting Information S1).

SS precursors from the 220-km discontinuity ($S_{220}S$) are observed on 2,756 seismograms. We are able to pick more $S_{220}S$ phases than $S_{LAB}S$ phases from seismograms partly because many $S_{LAB}S$ arrivals are too close to the main *SS* wave arrivals and they are not used in this study to avoid strong phase interferences. The $S_{LAB}S$ and $S_{220}S$ signals can be both clearly observed on 1,021 seismograms. There is no apparent geographic pattern associated with the presence (or absence) of the *SS* precursors (Figure 2). The amplitudes of the secondary reflected waves

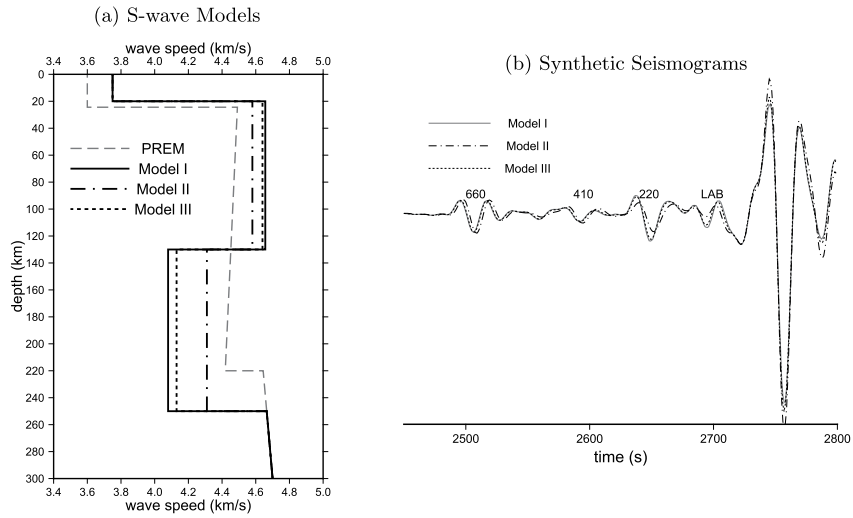

Figure 3. (a) Three 1-D reference earth models Model I, Model II, and Model III used in this study and their corresponding example synthetic seismograms are plotted in (b). Model PREM is also plotted in (a) for reference. The synthetic seismograms are calculated using the three reference models for a magnitude 6.9 Indonesia earthquake that occurred in August 2018 recorded at a GSN station SDDR (https://doi.org/10.7914/SN/CU). The observed seismogram is plotted in Figure 1. The seismograms have been band-pass filtered between 10 and 80 mHz and have been aligned using the main *SS* wave arrivals for better illustration. The velocity contrast across the lithenosphere–asthenosphere boundary at a depth of 130 km is 12.5% in Model I, 6% in Model II and 11% in Model III. The corresponding $S_{LAB}S$ wave amplitude in Model I is much larger than that in Model II and slightly larger than that in Model III, as expected.

are expected to be small, and the *SS* precursors are often below the noise level due to weak source radiation, small reflection coefficient and/or defocusing caused by mantle heterogeneities. For example, only about 30% of the recorded *SS* waves have clear *SS* precursors from the 410-km and the 660-km discontinuities in recent global studies (Guo & Zhou, 2020, 2021).

The observed *SS* precursors from the LAB ($S_{LAB}S$) are characterized by large amplitudes that are comparable to the amplitudes of the mantle transition zone *SS* precursors $S_{410}S$ and $S_{660}S$ (Figure 1). To investigate the velocity reduction across the LAB discontinuity, we construct 1-D reference models modified from PREM to include a large velocity drop in the asthenosphere (Figure 3 and Figure S4 of Supporting Information S1). We calculate synthetic seismograms based on traveling-wave mode summation (Liu & Zhou, 2016). The global centroid-moment-tensor solutions (Dziewonski et al., 1981; Ekström et al., 2012) and the USGS Preliminary Determination of Epicenters (USGS, 2017) source locations and origin times are used in the calculations of the 1-D synthetic seismograms. The synthetic seismograms are complete, including all seismic phases with exact amplitudes for earthquakes in 1-D earth models. The effects of incident angles on seismic amplitudes have been automatically accounted for. The synthetic seismograms are then processed using the same bandpass filter as applied to the observed seismograms. The differences in *SS* precursors between different models facilitate the identification of the $S_{LAB}S$ and $S_{220}S$ waves on the observed seismograms (Figure 3).

We measure the amplitudes of the *SS* precursors $S_{LAB}S$, $S_{410}S$, and $S_{660}S$ at a period of 25 s. The measurements are made in the frequency domain using a 40-s window centered at the arrival time of the *SS* precursors (Figure 4). We use a short time window to limit the interference between the $S_{LAB}S$ wave and the main *SS* wave. Example amplitude measurement experiments using synthetic data show that amplitude ratios at the measurement frequency as well as their frequency-dependent variations can be well captured using a 40-s time window (Figure 5). We will focus on measurements for a period of 25 s in this study. The longest half duration of the earthquakes used in this study is about 25 s and seismic energy often decreases rapidly at frequencies higher than the earthquake corner frequency. In addition, *SS* precursors at higher frequencies can be heavily contaminated by noises (meteorological and multiple scattering). At periods much longer than 25 s, seismograms are not suitable for *SS* precursor studies as the precursors are not well separated and surface-wave overtone dispersion also becomes a problem. The frequency dependence of the measurements and their corresponding finite-frequency sensitivities will be documented in a separate article. Amplitude ratios $S_{LAB}S/S_{410}S$ and $S_{LAB}S/S_{660}S$ are calculated for the observed datasets as well as synthetic seismograms in 1-D reference models (Figure 6).

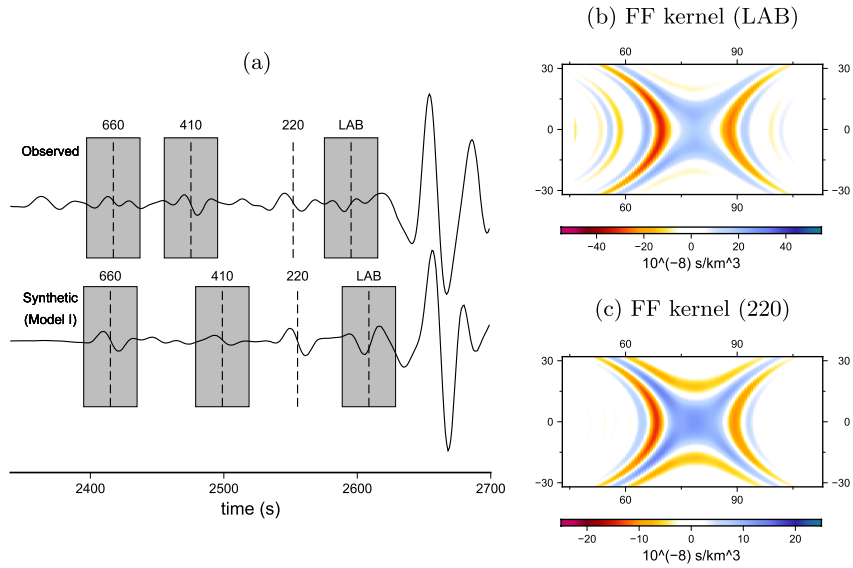

Figure 4. (a) shows example measurement windows used for lithenosphere–asthenosphere boundary amplitude ratio measurements $A_{S_{\mathrm{LAB}}S}/A_{S_{410}S}$ and $A_{S_{\mathrm{LAB}}S}/A_{S_{660}S}$. The seismograms are for a magnitude 6.6 Mexico earthquake occurred in January 2016 recorded at a GSN station MSEY (https://doi.org/10.7914/SN/II), and the epicentral distance is 158°. The synthetic seismogram is calculated for Model I as in Figure 3 and both seismograms have been band-pass filtered between 10 and 80 mHz. (b) and (c) are finite-frequency traveltime boundary sensitivity kernels for the $S_{\mathrm{LAB}}S$ and $S_{220}S$ waves, respectively. The sensitivity kernels are plotted in map view in the ray coordinates, centered at the bounce point which is about 79° away from the source and the receiver.

We measure the differential arrival times between the *SS* waves and their precursors in the dataset. The observed and synthetic seismograms are aligned using the *SS* traveltime measurements, and the residue arrival times of the *SS* precursors are then calculated in the frequency domain at a period of 25 s (Xue et al., 2015) (Figure 7). The time shifts due to uncertainties in source origin times do not affect the final measurements as only $\delta t|_{S_{\mathrm{LAB}}S} - \delta t|_{SS}$ and $\delta t|_{S_{220}S} - \delta t|_{SS}$ differential traveltimes are used to determine the depths of the discontinuities. The length of the measurement windows ranges from 42 to 117 s for *SS* waves, 37–69 s for $S_{\mathrm{LAB}}S$ waves, and 38–75 s for $S_{220}S$ waves. The length of a measurement window depends on the arrivals of the neighboring phases, and the measurement windows are chosen to minimize possible phase interferences. The relation between time delays and depth perturbations of the discontinuities depends on their finite-frequency sensitivity kernels. We calculate finite-frequency traveltime sensitivities to boundary depth perturbations in the framework of traveling-wave mode coupling, which fully accounts for source radiation patterns, phase interactions as well as time-domain windowing and tapering applied in making frequency-dependent measurements (Deng & Zhou, 2015; Zhou, 2009; Zhou et al., 2005). Example finite-frequency boundary sensitivity kernels for traveltime measurements are plotted in Figure 4. The finite-frequency sensitivities display a typical X shape due to the minimax-time nature of the reflected waves (Dahlen, 2005). Unlike direct body waves which have minimum-time ray paths, surface-reflected phases are minimax waves in that the reflection point is a stationary maximum for perturbations in the source-receiver ray plane and a minimum for perturbations perpendicular to the plane.

Seismic waves at different frequencies are sensitive to different regions (Fresnel zones) and this introduces frequency-dependent time shifts when lateral variations exist in discontinuity topography, as a result, *SS* precursors do not always have the same polarities as expected for 1-D earth models (Guo & Zhou, 2020). The interferences between different waves within the measurement window are accounted for in the calculation of the finite-frequency sensitivities, including the travel time curves of the interference phases as well as their amplitudes. We use traveltime sensitivity kernels to identify possible phase interferences in the measurement windows, including interferences with the main *SS* waves and other phases such as the precursors of depth phases (Figure S5 of Supporting Information S1), precursors and/or multiples of *ScS* waves (Figure S6 of Supporting Information S1). Sensitivity kernels with abnormal values indicate strong interferences and those measurements are excluded (Figures S5 and S6 of Supporting InformationS1). In addition, we exclude measurements out of the two standard deviations. This leaves 1,274 and 929 sets of measurements for $S_{\mathrm{LAB}}S$ and $S_{220}S$, respectively.

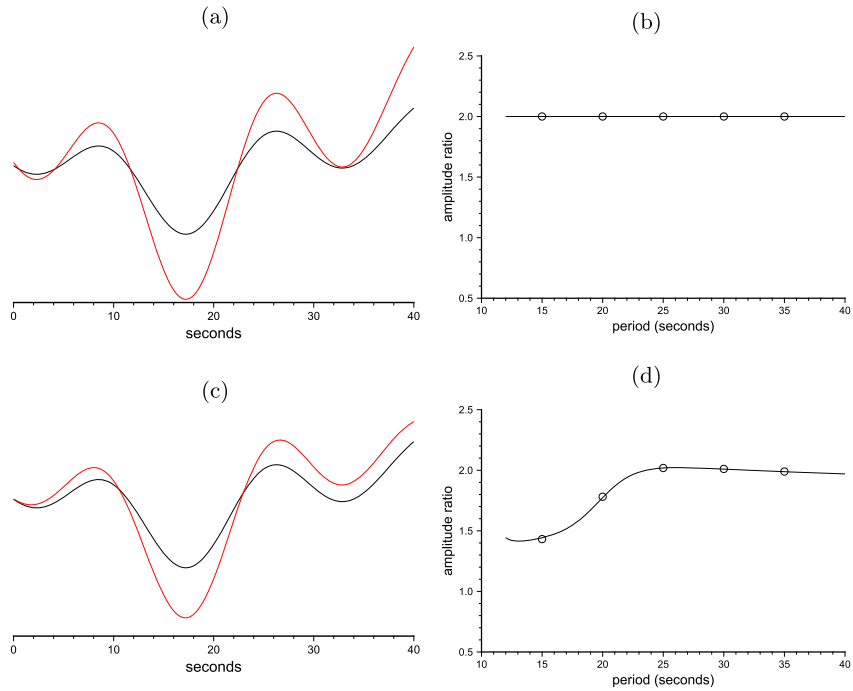

Figure 5. Synthetic amplitude measurement experiment using the same 40-s time window as applied in data. (a) The black seismogram is the lithenosphere–asthenosphere boundary phase from the observed seismogram in Figure 4, and we multiply the seismogram by a constant factor of two (frequency-independent) to obtain the red seismogram. (b) Theoretical amplitude spectral ratio (black line) and measurements made at periods of 15, 20, 25, 30, and 35 s (circles). (c) The black seismogram is the same as in (a) and the red seismogram is obtained by multiplying the amplitude spectrum of the black seismogram with a frequency-dependent function. The corresponding theoretical amplitude ratios and measurements made at 15, 20, 25, 30, and 35 s period are plotted in (d). The experiment confirms that amplitude ratios at the measurement frequency (25 s) can be determined using a 40-s time window.

The thicknesses of the asthenosphere at the 921 locations are calculated as the depth difference between the 220-km discontinuity and the LAB.

3. Results

We process a total number of 32,369 transverse component seismograms that have reflection points in oceanic regions and observe clear *SS* waves on 6,143 seismograms with simple source time functions. *SS* precursors are secondary reflected waves, their amplitudes are much smaller than the main *SS* waves and they are often heavily influenced by scattered waves and phase interactions. As expected, the majority of the seismograms with clear *SS* waves do not show strong *SS* precursors from the two discontinuities. The most striking observation from this dataset is the anomalously large amplitudes of the $S_{\mathrm{LAB}}S$ phases on 1,380 seismograms, with the majority (1,021 out of 1,380) accompanied by strong $S_{220}S$ phases. The *SS* precursors are well separated from the main *SS* waves, and their amplitudes are comparable to the amplitudes of the mantle transition zone phases, $S_{410}S$ and $S_{660}S$ (Figure 1). The geographic distribution of the reflection points is dispersive across major oceans, including the Pacific, the Atlantic, and the Indian Ocean, with seafloor age spanning from 10 to 170 million years old (Figure 1).

3.1. Large Amplitudes of the LAB *SS* Precursors

To quantify the observed large amplitudes of the *SS* precursors associated with the LAB discontinuity, we calculate the amplitude ratios between the $S_{\mathrm{LAB}}S$ phase and two reference phases, $S_{410}S$ and $S_{660}S$. The amplitude measurements are made in the frequency domain based on spectra division at a period of 25 s (Guo & Zhou, 2020; Xue et al., 2015), In Figure 6, we plot the histograms of the minimum amplitude ratios, defined as γ = minimum$[\log(A_{S_{\mathrm{LAB}}S}/A_{S_{410}S}), \log(A_{S_{\mathrm{LAB}}S}/A_{S_{660}S})]$. We have used the minimum values to avoid over-amplification

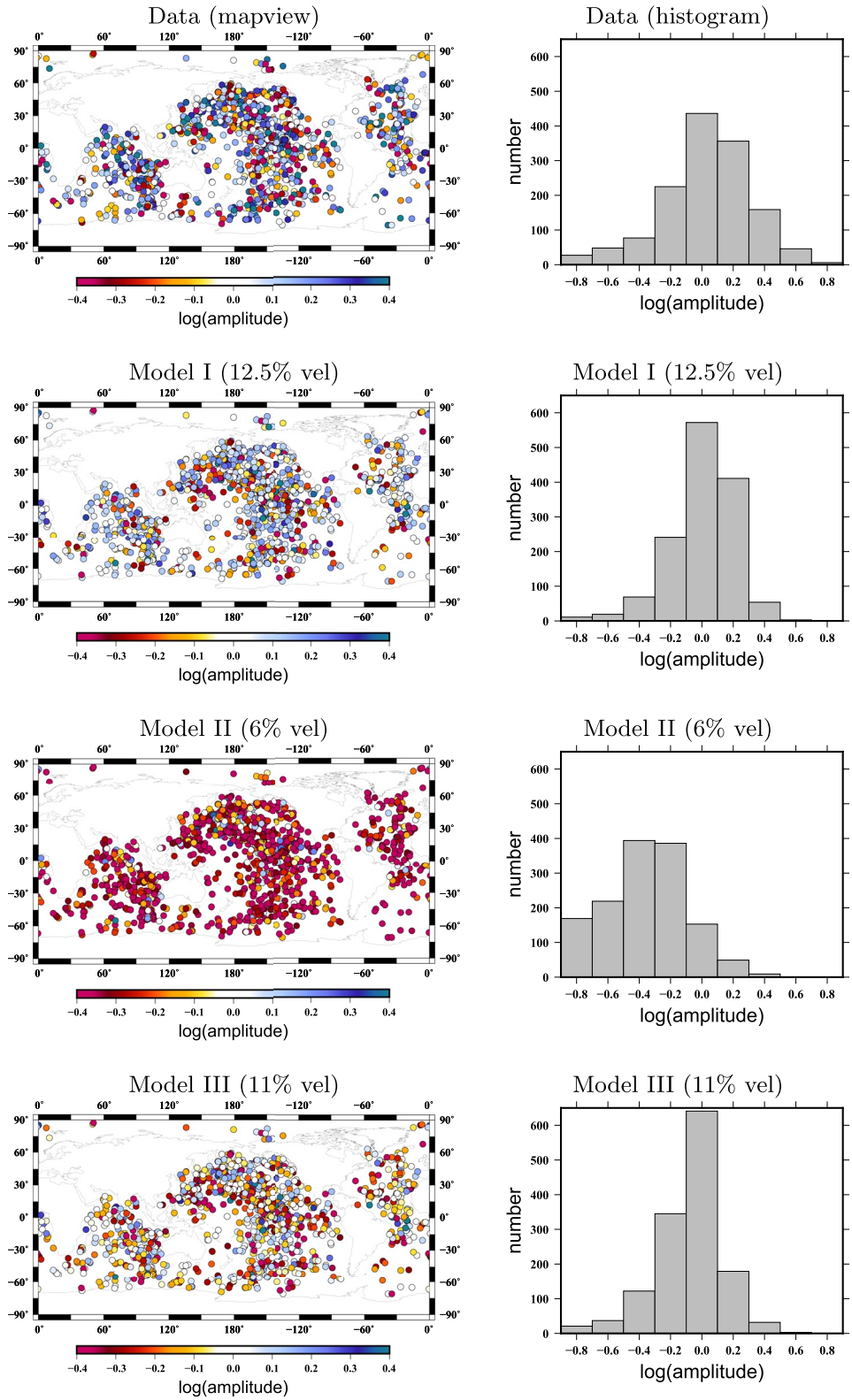

Figure 6.

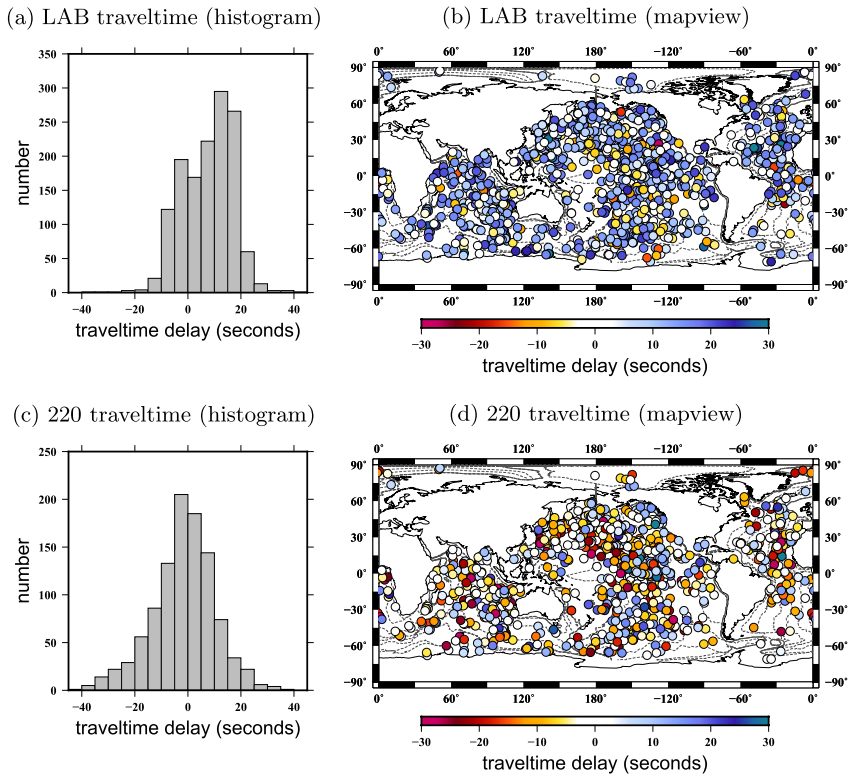

Figure 7. (a) and (b) are $S_{LAB}S$ traveltime measurements plotted in histograms and mapviews at their bounce points. The measurements are made with respect to Model I synthetic seismograms. 3-D mantle wavespeed and crustal corrections have been applied. (c) and (d) show the same as (a) and (b) but for $S_{220}S$.

when the amplitude of $S_{410}S$ or $S_{660}S$ is small due to scattering or defocusing. The precursor's $S_{LAB}S$ and $S_{410}S$ (or $S_{660}S$) have similar ray paths in the bulk mantle, the use of amplitude ratios minimizes the impact of possible focusing and defocusing effects. In addition, the main *SS* waves travel through the same regions sampled by the *SS* precursors, and the distribution of the *SS* amplitude measurements for the entire dataset is very similar to that for the subset in which anomalously large $S_{LAB}S$ were observed, indicating that the observed large amplitudes of the $S_{LAB}S$ waves are not a result of focusing caused by mantle heterogeneities (Figure S7 of Supporting Information S1). To investigate possible interference from the main *SS* waves and other phases on the frequency-domain $S_{LAB}S$ amplitude measurements, we make additional time-domain amplitude measurements using the maximum value of the envelope function for each $S_{LAB}S$ measurement window. The measurements made in the frequency domain based on spectra division and those made in the time domain using envelope functions, in general, agree well (Figure S8 of Supporting Information S1). The observed mean value of the minimum amplitude ratio γ is close to 0 (Figure 6), indicating that the reflection coefficients at the LAB are about the same as those at the 410 and the 660. The corresponding velocity contrasts across the LAB are expected to be larger than the contrasts across the 410 and the 660 due to their smaller incident angles at shallower depths. The geographic distribution of the amplitude ratios does not show dependence on the age of the sea floor (Figure 6).

To estimate the velocity change across the LAB, we construct a 1-D reference model with the depths of the LAB and the 220-km discontinuity at 130 and 250 km, respectively (Figure 3). The velocity jump across the LAB is 12.5% in the reference model (Model I). *SS* precursors from all upper mantle discontinuities can be clearly identified on the observed seismograms when the observed and synthetic seismograms are filtered to

Figure 6. $S_{LAB}S$ amplitude measurements γ = minimum $(\log(A_{S_{LAB}S}/A_{S_{410}S}), \log(A_{S_{LAB}S}/A_{S_{660}S}))$ obtained using observed seismograms (top) as well as synthetic seismograms calculated for three reference models (Model I, II, and III) plotted at the bounce points in mapviews and histograms. The observed $S_{LAB}S$ amplitudes show a similar distribution (histogram) to the amplitude ratios calculated for Model I (12.5% velocity drop across the lithenosphere–asthenosphere boundary [LAB]). The amplitude ratios calculated in Model II (6% velocity drop across the LAB) are overall much smaller than the observations, and the amplitude ratios calculated in Model III (11% velocity drop across the LAB) are slightly smaller than the observed amplitude ratios. We conclude that the observed large amplitude of the $S_{LAB}S$ waves can be explained by a 12.5% velocity drop across the LAB.

the same frequency band (Figure 1). We make amplitude measurements and calculate the relative amplitude ratios $\gamma = \text{minimum}[\log(A_{S_{\text{LAB}}S}/A_{S_{410}S}), \log(A_{S_{\text{LAB}}S}/A_{S_{660}S})]$ using the synthetic seismograms following the same process as applied on the observed seismograms. The amplitude ratios between $S_{\text{LAB}}S$ and $S_{410}S$ (or $S_{660}S$) calculated for Model I are very close to the observations (Figure 6). To better constrain the velocity drop across the LAB required to produce the large amplitudes of $S_{\text{LAB}}S$, we introduce two additional models, Model II with 6% of velocity drop and Model III with 11% of velocity drop across the LAB. Example synthetic seismograms are plotted in Figure 3 and the amplitude measurements are plotted in Figure 6. The mean logarithm amplitude ratio γ calculated using Model II as a reference model is −0.3, meaning that the corresponding average amplitudes of the LAB precursors are about 50% of the amplitudes of the 410 (or the 660) precursors, much smaller than the observations. The mean logarithm amplitude ratio γ calculated using Model III as a reference model is slightly smaller than the observed value. Based on the calculations, we conclude that a 12.5% of velocity drop across the LAB is necessary for our model to explain the observed large amplitude of the $S_{\text{LAB}}S$ waves (Figure 6).

3.2. Depths of the LAB and the 220-km Discontinuity

To constrain the depths of the LAB and the 220-km discontinuity, we measure the differential traveltimes $\delta t|_{S_{\text{LAB}}S} - \delta t|_{SS}$ and $\delta t|_{S_{220}S} - \delta t|_{SS}$ with respect to synthetic seismograms calculated in Model I (Figure 7), similar to the studies of Guo and Zhou (2020, 2021) in which $S_{410}S$ and $S_{660}S$ traveltime measurements were used to investigate the depths of the 410-km and the 660-km discontinuities at a global scale. The time shifts due to uncertainties in source origin times do not affect the final measurements as we use differential traveltimes. We apply 3-D crust and mantle wave speed corrections using global models CRUST1.0 (Laske et al., 2013) and S40RTS (Ritsema et al., 2011). Model I is constructed as the reference model for the oceanic regions where large-amplitude *SS* precursors have been observed. As it is not a global reference model, there are overall about 5 s of traveltime shifts in $\delta t|_{S_{\text{LAB}}S}$-$\delta t|_{SS}$ after 3-D wavespeed and crustal corrections (Figure 7 and Figure S9 of Supporting Information S1). The mean $\delta t|_{S_{220}S}$-$\delta t|_{SS}$ traveltime delay before and after the corrections remains approximately the same, with an average value close to zero. This indicates that the average velocity in the uppermost mantle in the reference model is close to the global average.

To obtain depth perturbations of the LAB and the 220-km discontinuity, we calculate the sensitivities of the differential traveltimes to depth perturbations of the interfaces by integrating the finite-frequency sensitivity kernels over the surface of the boundary (Figure 4). The LAB depths obtained from this study varies between ∼70 and ∼160 km (Figure 8) and the mean LAB depths obtained using the same data with and without the corrections are 120 and 125 km, respectively (Figure 8 and Figure S10 of Supporting Information S1). The depth of the 220-km discontinuity varies between 180 and 340 km with a mean value of ∼255 km, and it does not change with wavespeed and crustal corrections. We calculate the thickness of the asthenosphere in regions where both the LAB and the 220-km discontinuities are well-defined by strong *SS* precursors from both discontinuities. The thickness of the asthenosphere ranges from 50 to 220 km with an average of 140 km. Large depth variations of the LAB and the 220-km discontinuity are observed across the global oceanic regions and the depth can change abruptly over small geographic distances.

The depths of the LAB and the 220-km discontinuity are plotted as a function of seafloor age (Müller et al., 2019) in Figure 9. The depths of the two discontinuities obtained using the same dataset but without the 3-D crustal and mantle wave speed corrections are plotted in Figure S11 of Supporting Information S1. The average depth of the two discontinuities is independent of seafloor age, regardless of the corrections applied. To quantify uncertainties in traveltime measurements and discontinuity depth perturbations, we calculate frequency-dependent traveltime measurements at five different periods ranging from 23 to 27 s. The standard deviation of those traveltime measurements is then converted to uncertainties in discontinuity depth using the corresponding finite-frequency sensitivities. The depth uncertainties are plotted as error bars in Figure 9, they are generally small, with an average of 1.1 km for the LAB and 1.2 km for the 220-km discontinuity.

4. Discussions

4.1. Melt Spots in the Oceanic Asthenosphere

The observed large amplitudes of the *SS* precursors require a large velocity change across the LAB. The presence of a small amount of melt may significantly reduce seismic velocity (Liu & King, 2022). It has been

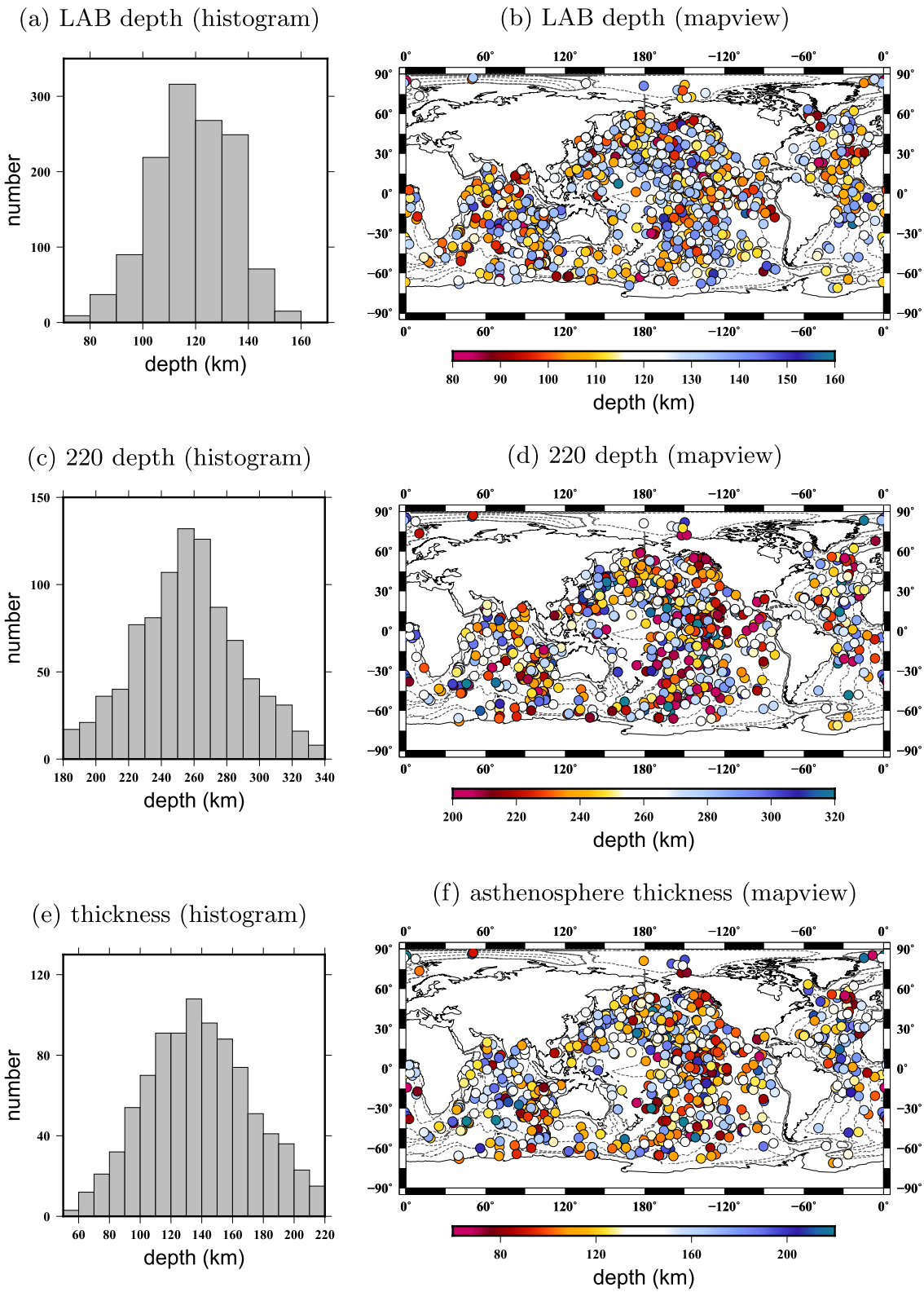

Figure 8. (a) and (b) are the depths of the lithenosphere–asthenosphere boundary (LAB) calculated from traveltime measurements, plotted in histogram and mapview at $S_{LAB}S$ bounce points. (c) and (d) are the depths of the 220-km discontinuity. (e) and (f) are the asthenosphere thicknesses calculated from the depths of the LAB and the 220.

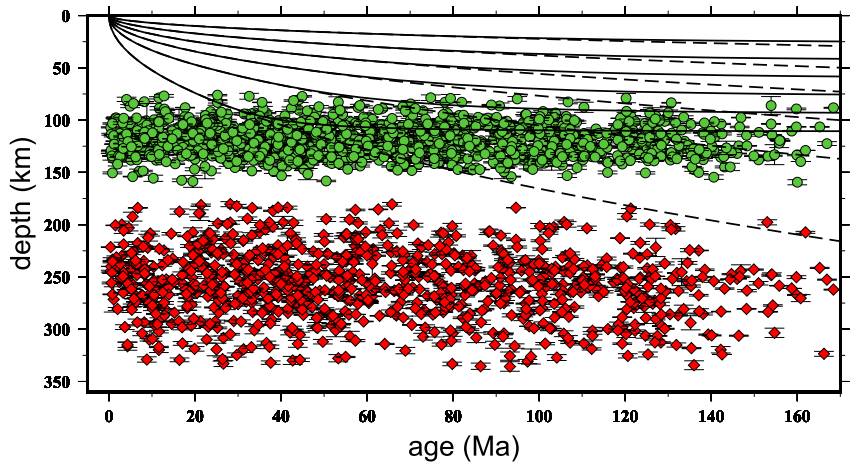

Figure 9. Age-independent thickness of the oceanic plate. Green circles and red diamonds are depths of the lithenosphere–asthenosphere boundary (LAB) and the 220-km discontinuity obtained from this study, plotted as a function of the seafloor age. Isotherms at an interval of 200°C (starting at 300°C) from the half space cooling model (dashed line) and the plate model (solid line) are plotted for reference. The observed depths of the two discontinuities show significant local variations. The average depths of the LAB and the 220-km discontinuity are at 120 and 255 km, independent of seafloor age. The depth uncertainties estimated from frequency-dependent measurements are plotted as error bars.

suggested that S-wave velocity reduction is about 7.9% for every percent of melt in realistically shaped melt in the upper mantle based on finite element calculations for shear modulus reduction (produced by the presence of a connected network of realistically shaped and naturally organized melt inclusions), with the geometries of the inclusions taken directly from laboratory calculations (Hammond & Humphreys, 2000). The finite element model predictions are also in general agreement with recent experimental results (Chantel et al., 2016). The large amplitudes of the *SS* precursors observed in this study can be explained by 1.5%–2% of melt in the asthenosphere. This melt concentration is comparable to observations at mid-ocean ridges, for example, the East Pacific Rise (The MELT Seismic Team, 1998). In a recent surface-wave study (Debayle et al., 2020), a large melt fraction of up to 1% beneath the entire oceanic lithosphere has been suggested, in general agreement with the overall estimation of melt (0.3%–2%) from electrical conductivity study (Ni et al., 2011).

A sharp increase in the water content across the LAB has been proposed as a possible candidate for significant wave speed reduction through enhanced anelasticity (Karato, 2012; Karato & Jung, 1998). To explore the effect of anelasticity (seismic quality factor Q) on the amplitudes of *SS* precursors, we calculate synthetic seismograms in models with and without strong anelasticity in the asthenosphere and compare the amplitudes of the *SS* precursors. In Figure 10, the velocity and density structures in Model I and Model IV are identical (Figure S4 of Supporting Information S1) but their Q values in the asthenosphere are different, $Q = 80$ in Model I and $Q = 20$ in Model IV. The low Q value in the asthenosphere in Model IV results in a much smaller *SS* amplitude but the amplitude reduction on the $S_{LAB}S$ wave is very limited. This is because while both the *SS* wave and the $S_{LAB}S$ wave experience more attenuation due to enhanced anelasticity, anelasticity also reduces the effective wave speed in the low Q region. Therefore, the effective velocity contrast across the LAB increases, resulting in a larger reflection coefficient and increased amplitude of the $S_{LAB}S$ wave. The amplitude ratios calculated in Model I (Figure 6) and Model IV (Figure 10) do not show significant differences in their histograms. We conclude that the large amplitudes of $S_{LAB}S$ waves therefore can not be explained by a change in anelasticity.

The observed large amplitudes of the *SS* precursors can not be explained by seismic anisotropy. Strong radial anisotropy (up to 10%) has been observed in the oceanic asthenosphere with SH waves traveling faster than SV waves (Beghein et al., 2014; Burgos et al., 2014; Dziewonski & Anderson, 1981; Nettles & Dziewoński, 2008; Zhou et al., 2006). This radial anisotropy would lead to larger SH wave velocity beneath the LAB, and therefore reduced velocity contrast across the LAB and smaller precursor amplitudes, while the observed large amplitudes of the *SS* precursors require anomalously large velocity drop (12.5%) across the boundary. Frozen-in radial anisotropy in the oceanic lithosphere from petrological fabrics or melt ponding has been suggested (Auer et al., 2015). In this case, the SH wave speed would become faster in the oceanic lithosphere, which may cause a larger SH velocity contrast across the LAB but a reduced velocity contrast in SV velocity. In this study, strong $S_{LAB}S$

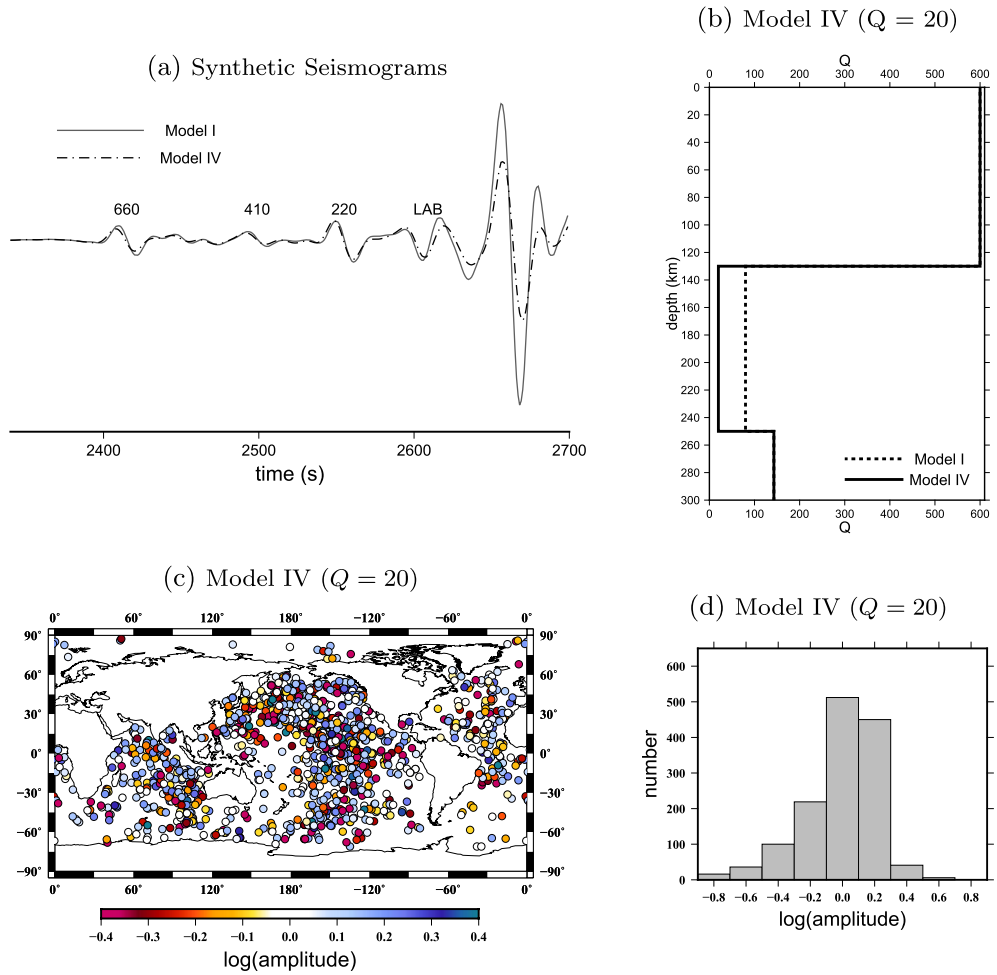

Figure 10. (a) Synthetic seismograms calculate for Model I and Model IV as in Figure 3. (b) Q structure in the 1-D reference models Model I and Model IV. Model IV is identical to Model I in velocity and density but has a much smaller Q value ($Q = 20$) in the asthenosphere than in Model I ($Q = 80$). The amplitude of the main SS wave becomes smaller in Model IV synthetics due to the overall stronger attenuation associated with the lower Q value in the asthenosphere but its impact on the amplitude of the SS precursor $S_{LAB}S$ is very limited. This is because anelasticity also reduces the effective wave speed in the low Q region. Therefore, velocity contrast across the lithenosphere–asthenosphere boundary increases, resulting a larger reflection coefficient which increases the amplitude of the $S_{LAB}S$ wave. The observed large amplitudes of the $S_{LAB}S$ waves therefore can not be fully explained by a reduction of Q values in the asthenosphere.

phases are also observed on the radial component seismograms (Figure S12 of Supporting Information S1). The observed SS precursors with large amplitudes also display a good azimuth coverage (Figure 1), indicating that the observed large amplitudes of the $S_{LAB}S$ waves are unlikely a result of azimuth anisotropy in the lithosphere (Beghein et al., 2014).

It is important to emphasize that we have interpreted the LVZ between the two discontinuities observed in oceanic regions as the asthenosphere, and we have modeled the wavespeed structure associated with reflected waves as first-order discontinuities. In 1-D earth models (e.g., PREM), a first-order discontinuity is an equivalent mathematical representation of the earth structure. The same applies to other discontinuities in the Earth including the Moho, the 410 and the 660. Synthetic seismograms calculated based on the equivalent first-order discontinuities can explain the observed seismograms. The large amplitude of the LAB phase observed in this study requires about a 12.5% velocity jump across a first-order discontinuity. The same velocity change over a gradient zone of 5 km or less may also explain the observed $S_{LAB}S$ amplitudes, with less than 2% of the difference in their average amplitudes (Figure S13). If the velocity change occurs over a much larger gradient zone of 20 km, the average $S_{LAB}S$ amplitude will decrease by ~17%, and the required velocity increase would be larger in order to produce the same peak amplitude (Deng & Zhou, 2015).

4.2. Age-Independent Thickness of the Oceanic Plate

The observed LAB *SS* precursors characterized by large amplitudes can be modeled as waves reflected off a first-order discontinuity with a large velocity contrast. The strong *SS* precursors from the LAB are observed across the global oceanic regions, with an average depth of 120 km that is independent of seafloor age (Figure 9). This observation supports the plate model for the oceanic bathymetry and heat flow measurements, in which a reheating process is required at the base of the oceanic plate with a constant thickness of about 100–125 km. The reheating process is probably caused by small-scale mantle convection beneath the large oceanic plate (Richards et al., 2020).

The observed depths of the LAB in this study are characterized by substantial local variations. The standard deviation of the LAB depths calculated for the entire dataset is ∼15 km. We calculate the standard deviation of the LAB depths at different length scales (Figure S14 of Supporting Information S1). The standard deviation can be up to ∼17 km at small length scales and it becomes consistent with the standard deviation of the entire dataset when the length scale exceeds ∼1,000 km. Reflectors at depths between 120 and 180 km have been detected across the Pacific Ocean in a *SS* precursor stacking study, though they were found in only 16% of the stacks (Schmerr, 2012). LAB reflectors at depths of about 100–140 km have been reported in Hawaii where high-resolution receiver function studies are available with the deployment of local stations (Li et al., 2000, 2004). The large variation of the LAB depths is also consistent with surface wave studies in which individual transects often display considerable depth variability in age-averaged profiles (French et al., 2013; Rychert et al., 2020).

In seismic studies, age-dependent reflectors have been reported in several oceanic regions, especially under the young seafloors (Rychert et al., 2021; Rychert & Shearer, 2011; Tharimena et al., 2017; Wang et al., 2020). For example, a recent receiver function study from ocean bottom seismometers in the equatorial Mid-Atlantic Ocean discovered that the LAB depth increases from about 30 km at the mid-ocean ridge to about 80 km beneath 30 million years old seafloors in some locations (Rychert et al., 2021). The relation between the crust age and the LAB depth is much less clear across the Pacific Ocean and it has been suggested that regional dynamical processes may play an important role in asthenospheric melt production (Schmerr, 2012). In this study, we use long period *SS* waves, as a result, signals from a very shallow reflector (<40 km) will interfere with the main *SS* waves and will not be picked up. It is also possible that there may be multiple reflectors in the lithosphere in some regions and what we observe in this study represents a strong deep reflector associated with melting not secular cooling. In general, velocity change associated with a thermal lithosphere is expected to be smaller and much more gradual than the reflectors associated with the chemical differentiation (melting) process.

Similar to the LAB, the depths of the 220-km discontinuity also do not depend on the age of the seafloor and are characterized by large local variations. It is understood that the smoothness (roughness) of the same discontinuity in different studies often depends on the regions of study as well as the smoothing applied in some of the inversions. Reflectors at depths of 250–300 km (the X discontinuity) have been observed in many oceanic regions, including the South Pacific and the Indian Ocean (Deuss & Woodhouse, 2002, 2004). Large depth variations up to ∼100 km on the 220-km discontinuity have been reported over length scales of several hundred kilometers beneath the northwestern Pacific in a short-period array study (Rost & Weber, 2001). The large local variations in the depths of the discontinuities are expected to generate significant variability in both the waveforms and travel times of the *SS* precursors. When stacking is applied to *SS* precursors with reflection points in regions where large depth variations occur over very short distances, it may be possible that the large amplitudes of *SS* precursors could be effectively averaged out in stacking results due to phase equalization (Gu et al., 2001). In Figure S15 of Supporting Information S1, we show a simple example to illustrate the concept that, in some cases, the large amplitudes of *SS* precursors may not be picked up in stacking results when large variations in *SS* precursor amplitudes and arrival times are present.

5. Conclusions

The thermal boundary as predicted by the half space cooling model is not observed in *SS* precursors in this study. Instead, we observe anomalously large amplitudes of *SS* precursors reflected off the LAB, which can be explained by ∼12.5% velocity drop across the boundary. This indicates 1.5%–2% of localized melt across the global oceanic regions. The large variability in the depths and amplitudes of the *SS* precursors observed across the global oceanic region suggests a heterogeneous melting process in the oceanic asthenosphere. The majority

of the LAB *SS* precursors are accompanied by strong reflections from the 220-km discontinuity. This indicates that the 220-km discontinuity may define the lower boundary of the local asthenosphere where melting occurs.

The plate model, which requires additional heat at the base of a constant-thickness oceanic plate, explains the bathymetry and heat flow observations that do not follow half space cooling predictions. While such a constant-thickness plate has not been reported in seismic studies, the oceanic plate as defined by the strong LAB reflector in this study does not thicken with age but shows an average depth of 120 km across different age bands. This observation supports the existence of a constant-thickness plate in oceanic regions. The localized melt spots distributed over the global oceanic regions may be essential to decouple the oceanic plates from the underlying mantle by dramatically reducing the mantle viscosity (Debayle et al., 2020; Holtzman, 2016).

Data Availability Statement

Raw seismic waveforms used in this study are available from the IRIS platform (https://ds.iris.edu/ds/nodes/dmc/). All GSN stations were used. The network codes are CU (https://doi.org/10.7914/sn/cu), GT (https://doi.org/10.7914/sn/gt), IC (https://doi.org/10.7914/sn/ic), II (https://doi.org/10.7914/sn/ii), IU (https://doi.org/10.7914/sn/iu). Data preparation and preprocessing were performed using the Seismic Analysis Code (Goldstein et al., 2003; Goldstein & Snoke, 2005) (https://ds.iris.edu/ds/nodes/dmc/software/downloads/sac/). Figures were made with the Generic Mapping Tools (GMT) package (Wessel & Smith, 1995). Data products from this study including measurements and models can be downloaded from https://doi.org/10.5281/zenodo.7482556.

Acknowledgments
We thank the Editor Dr. Douglas Schmitt, the Associate Editor and an anonymous reviewer for their constructive comments, which helped improve the manuscript. The facilities of the IRIS Data Management System, and specifically the IRIS Data Management Center, were used for access to waveform and metadata required in this study. We used data from the Global Seismographic Network (GSN), which is a cooperative scientific facility operated jointly by the National Science Foundation (NSF) and the United States Geological Survey (USGS). The NSF component is part of NSF's SAGE facility, operated by the Incorporated Research Institutions for Seismology (IRIS) under Cooperative Support Agreement EAR-1851048. The authors acknowledge Advanced Research Computing at Virginia Tech for providing computational resources and technical support. This research was supported by the US National Science Foundation under Grant EAR-2017218.

References

Auer, L., Becker, T. W., Boschi, L., & Schmerr, N. (2015). Thermal structure, radial anisotropy, and dynamics of oceanic boundary layers. *Geophysical Research Letters*, *42*(22), 9740–9749. https://doi.org/10.1002/2015gl066246

Beghein, C., Yuan, K., Schmerr, N., & Xing, Z. (2014). Changes in seismic anisotropy shed light on the nature of the gutenberg discontinuity. *Science*, *343*(6176), 1237–1240. https://doi.org/10.1126/science.1246724

Burgos, G., Montagner, J.-P., Beucler, E., Capdeville, Y., Mocquet, A., & Drilleau, M. (2014). Oceanic lithosphere-asthenosphere boundary from surface wave dispersion data. *Journal of Geophysical Research: Solid Earth*, *119*(2), 1079–1093. https://doi.org/10.1002/2013jb010528

Chantel, J., Manthilake, G., Andrault, D., Novella, D., Yu, T., & Wang, Y. (2016). Experimental evidence supports mantle partial melting in the asthenosphere. *Science Advances*, *2*(5), e1600246. https://doi.org/10.1126/sciadv.1600246

Dahlen, F. (2005). Finite-frequency sensitivity kernels for boundary topography perturbations. *Geophysical Journal International*, *162*(2), 525–540. https://doi.org/10.1111/j.1365-246x.2005.02682.x

Debayle, E., Bodin, T., Durand, S., & Ricard, Y. (2020). Seismic evidence for partial melt below tectonic plates. *Nature*, *586*(7830), 555–559. https://doi.org/10.1038/s41586-020-2809-4

Deng, K., & Zhou, Y. (2015). Wave diffraction and resolution of mantle transition zone discontinuities in receiver function imaging. *Geophysical Journal International*, *201*(3), 2008–2025. https://doi.org/10.1093/gji/ggv124

Deuss, A., & Woodhouse, J. H. (2002). A systematic search for mantle discontinuities using ss-precursors. *Geophysical Research Letters*, *29*(8), 90–91. https://doi.org/10.1029/2002gl014768

Deuss, A., & Woodhouse, J. H. (2004). The nature of the lehmann discontinuity from its seismological clapeyron slopes. *Earth and Planetary Science Letters*, *225*(3–4), 295–304. https://doi.org/10.1016/j.epsl.2004.06.021

Dziewonski, A. M., & Anderson, D. L. (1981). Preliminary reference Earth model. *Physics of the Earth and Planetary Interiors*, *25*(4), 297–356. https://doi.org/10.1016/0031-9201(81)90046-7

Dziewonski, A. M., Chou, T.-A., & Woodhouse, J. H. (1981). Determination of earthquake source parameters from waveform data for studies of global and regional seismicity. *Journal of Geophysical Research*, *86*(B4), 2825–2852. https://doi.org/10.1029/jb086ib04p02825

Ekström, G., Nettles, M., & Dziewoński, A. (2012). The global cmt project 2004–2010: Centroid-moment tensors for 13,017 earthquakes. *Physics of the Earth and Planetary Interiors*, *200*, 1–9. https://doi.org/10.1016/j.pepi.2012.04.002

Faul, U. H., & Jackson, I. (2005). The seismological signature of temperature and grain size variations in the upper mantle. *Earth and Planetary Science Letters*, *234*(1–2), 119–134. https://doi.org/10.1016/j.epsl.2005.02.008

Fischer, K. M., Ford, H. A., Abt, D. L., & Rychert, C. A. (2010). The lithosphere-asthenosphere boundary. *Annual Review of Earth and Planetary Sciences*, *38*(1), 551–575. https://doi.org/10.1146/annurev-earth-040809-152438

Fischer, K. M., Rychert, C. A., Dalton, C. A., Miller, M. S., Beghein, C., & Schutt, D. L. (2020). A comparison of oceanic and continental mantle lithosphere. *Physics of the Earth and Planetary Interiors*, *309*, 106600. https://doi.org/10.1016/j.pepi.2020.106600

French, S., Lekic, V., & Romanowicz, B. (2013). Waveform tomography reveals channeled flow at the base of the oceanic asthenosphere. *Science*, *342*(6155), 227–230. https://doi.org/10.1126/science.1241514

Gaherty, J. B., & Jordan, T. H. (1995). Lehmann discontinuity as the base of an anisotropic layer beneath continents. *Science*, *268*(5216), 1468–1471. https://doi.org/10.1126/science.268.5216.1468

Godfrey, K. E., Dalton, C. A., & Ritsema, J. (2017). Seafloor age dependence of rayleigh wave phase velocities in the indian ocean. *Geochemistry, Geophysics, Geosystems*, *18*(5), 1926–1942. https://doi.org/10.1002/2017gc006824

Goldstein, P., Dodge, D., Firpo, M., Minner, L., Lee, W., Kanamori, H., et al. (2003). Sac2000: Signal processing and analysis tools for seismologists and engineers. *The IASPEI international handbook of earthquake and engineering seismology*, *81*, 1613–1620.

Goldstein, P., & Snoke, A. (2005). Sac availability for the iris community. Incorporated research Institutions for seismology Newsletter (Vol. *7*). UCRL-JRNL-211140).

Goncz, J. H., & Cleary, J. R. (1976). Variations in the structure of the upper mantle beneath Australia, from rayleigh wave observations. *Geophysical Journal International*, *44*(2), 507–516. https://doi.org/10.1111/j.1365-246x.1976.tb03670.x

Gu, Y. J., Dziewonski, A. M., & Ekström, G. (2001). Preferential detection of the lehmann discontinuity beneath continents. *Geophysical Research Letters*, *28*(24), 4655–4658. https://doi.org/10.1029/2001gl013679
Guo, Z., & Zhou, Y. (2020). Finite-frequency imaging of the global 410-and 660-km discontinuities using ss precursors. *Geophysical Journal International*, *220*(3), 1978–1994. https://doi.org/10.1093/gji/ggz546
Guo, Z., & Zhou, Y. (2021). Stagnant slabs and their return flows from finite-frequency tomography of the 410-km and 660-km discontinuities. *Journal of Geophysical Research: Solid Earth*, *126*(5), e2020JB021099. https://doi.org/10.1029/2020jb021099
Hales, A., Muirhead, K., & Rynn, J. (1980). A compressional velocity distribution for the upper mantle. *Tectonophysics*, *63*(1–4), 309–348. https://doi.org/10.1016/0040-1951(80)90119-5
Hammond, W. C., & Humphreys, E. D. (2000). Upper mantle seismic wave velocity: Effects of realistic partial melt geometries. *Journal of Geophysical Research*, *105*(B5), 10975–10986. https://doi.org/10.1029/2000jb900041
Holtzman, B. K. (2016). Questions on the existence, persistence, and mechanical effects of a very small melt fraction in the asthenosphere. *Geochemistry, Geophysics, Geosystems*, *17*(2), 470–484. https://doi.org/10.1002/2015gc006102
James, E. K., Dalton, C. A., & Gaherty, J. B. (2014). Rayleigh wave phase velocities in the Atlantic upper mantle. *Geochemistry, Geophysics, Geosystems*, *15*(11), 4305–4324. https://doi.org/10.1002/2014gc005518
Karato, S.-i. (1992). On the lehmann discontinuity. *Geophysical Research Letters*, *19*(22), 2255–2258. https://doi.org/10.1029/92gl02603
Karato, S.-i. (2012). On the origin of the asthenosphere. *Earth and Planetary Science Letters*, *321*, 95–103. https://doi.org/10.1016/j.epsl.2012.01.001
Karato, S.-i., & Jung, H. (1998). Water, partial melting and the origin of the seismic low velocity and high attenuation zone in the upper mantle. *Earth and Planetary Science Letters*, *157*(3–4), 193–207. https://doi.org/10.1016/s0012-821x(98)00034-x
Karato, S.-i., & Wu, P. (1993). Rheology of the upper mantle: A synthesis. *Science*, *260*(5109), 771–778. https://doi.org/10.1126/science.260.5109.771
Kawakatsu, H., Kumar, P., Takei, Y., Shinohara, M., Kanazawa, T., Araki, E., & Suyehiro, K. (2009). Seismic evidence for sharp lithosphere-asthenosphere boundaries of oceanic plates. *Science*, *324*(5926), 499–502. https://doi.org/10.1126/science.1169499
Kawakatsu, H., & Utada, H. (2017). Seismic and electrical signatures of the lithosphere–asthenosphere system of the normal oceanic mantle. *Annual Review of Earth and Planetary Sciences*, *45*(1), 139–167. https://doi.org/10.1146/annurev-earth-063016-020319
Korenaga, T., & Korenaga, J. (2008). Subsidence of normal oceanic lithosphere, apparent thermal expansivity, and seafloor flattening. *Earth and Planetary Science Letters*, *268*(1–2), 41–51. https://doi.org/10.1016/j.epsl.2007.12.022
Laske, G., Masters, G., Ma, Z., & Pasyanos, M. (2013). Update on crust1. 0—A 1-degree global model of Earth's crust. *Geophysical Research Abstracts*, *15*, 2658.
Lehmann, I. (1959). Velocities of longitudinal waves in the upper part of the Earth's mantle. *Annales de Geophysique*, *15*, 93.
Lehmann, I. (1961). S and the structure of the upper mantle. *Geophysical Journal International*, *4*(Supplement_1), 124–138. https://doi.org/10.1111/j.1365-246x.1961.tb06808.x
Li, X., Kind, R., Priestley, K., Sobolev, S. V., Tilmann, F., Yuan, X., & Weber, M. (2000). Mapping the Hawaiian plume conduit with converted seismic waves. *Nature*, *405*(6789), 938–941. https://doi.org/10.1038/35016054
Li, X., Kind, R., Yuan, X., Wölbern, I., & Hanka, W. (2004). Rejuvenation of the lithosphere by the Hawaiian plume. *Nature*, *427*(6977), 827–829. https://doi.org/10.1038/nature02349
Liu, K., & Zhou, Y. (2016). Travelling-wave green tensor and near-field rayleigh-wave sensitivity. *Geophysical Supplements to the Monthly Notices of the Royal Astronomical Society*, *205*(1), 134–145. https://doi.org/10.1093/gji/ggv564
Liu, S., & King, S. D. (2022). Dynamics of the North American plate: Large-scale driving mechanism from far-field slabs and the interpretation of shallow negative seismic anomalies. *Geochemistry, Geophysics, Geosystems*, *23*(3), e2021GC009808. https://doi.org/10.1029/2021GC009808
Ma, Z., & Dalton, C. A. (2019). Evidence for dehydration-modulated small-scale convection in the oceanic upper mantle from seafloor bathymetry and rayleigh wave phase velocity. *Earth and Planetary Science Letters*, *510*, 12–25. https://doi.org/10.1016/j.epsl.2018.12.030
Maggi, A., Debayle, E., Priestley, K., & Barruol, G. (2006). Multimode surface waveform tomography of the Pacific ocean: A closer look at the lithospheric cooling signature. *Geophysical Journal International*, *166*(3), 1384–1397. https://doi.org/10.1111/j.1365-246x.2006.03037.x
Mehouachi, F., & Singh, S. C. (2018). Water-rich sublithospheric melt channel in the equatorial atlantic ocean. *Nature Geoscience*, *11*(1), 65–69. https://doi.org/10.1038/s41561-017-0034-z
Müller, R. D., Zahirovic, S., Williams, S. E., Cannon, J., Seton, M., Bower, D. J., et al. (2019). A global plate model including lithospheric deformation along major rifts and orogens since the triassic. *Tectonics*, *38*(6), 1884–1907. https://doi.org/10.1029/2018tc005462
Nettles, M., & Dziewoński, A. M. (2008). Radially anisotropic shear velocity structure of the upper mantle globally and beneath North America. *Journal of Geophysical Research*, *113*(B2), B02303. https://doi.org/10.1029/2006jb004819
Ni, H., Keppler, H., & Behrens, H. (2011). Electrical conductivity of hydrous basaltic melts: Implications for partial melting in the upper mantle. *Contributions to Mineralogy and Petrology*, *162*(3), 637–650. https://doi.org/10.1007/s00410-011-0617-4
Parsons, B., & Sclater, J. G. (1977). An analysis of the variation of ocean floor bathymetry and heat flow with age. *Journal of Geophysical Research*, *82*(5), 803–827. https://doi.org/10.1029/jb082i005p00803
Revenaugh, J., & Jordan, T. H. (1991). Mantle layering from scs reverberations: 3. The upper mantle. *Journal of Geophysical Research*, *96*(B12), 19781–19810. https://doi.org/10.1029/91jb01487
Richards, F., Hoggard, M., Crosby, A., Ghelichkhan, S., & White, N. (2020). Structure and dynamics of the oceanic lithosphere-asthenosphere system. *Physics of the Earth and Planetary Interiors*, *309*, 106559. https://doi.org/10.1016/j.pepi.2020.106559
Richter, F. M. (1973). Convection and the large-scale circulation of the mantle. *Journal of Geophysical Research*, *78*(35), 8735–8745. https://doi.org/10.1029/jb078i035p08735
Richter, F. M., & Parsons, B. (1975). On the interaction of two scales of convection in the mantle. *Journal of Geophysical Research*, *80*(17), 2529–2541. https://doi.org/10.1029/jb080i017p02529
Ritsema, J., Deuss, a. A., Van Heijst, H., & Woodhouse, J. (2011). S40rts: A degree-40 shear-velocity model for the mantle from new rayleigh wave dispersion, teleseismic traveltime and normal-mode splitting function measurements. *Geophysical Journal International*, *184*(3), 1223–1236. https://doi.org/10.1111/j.1365-246x.2010.04884.x
Rost, S., & Weber, M. (2001). A reflector at 200 km depth beneath the northwest Pacific. *Geophysical Journal International*, *147*(1), 12–28. https://doi.org/10.1046/j.1365-246x.2001.00497.x
Rychert, C. A., Harmon, N., Constable, S., & Wang, S. (2020). The nature of the lithosphere-asthenosphere boundary. *Journal of Geophysical Research: Solid Earth*, *125*(10), e2018JB016463. https://doi.org/10.1029/2018jb016463
Rychert, C. A., Schmerr, N., & Harmon, N. (2012). The Pacific lithosphere-asthenosphere boundary: Seismic imaging and anisotropic constraints from ss waveforms. *Geochemistry, Geophysics, Geosystems*, *13*(9). https://doi.org/10.1029/2012gc004194

Rychert, C. A., & Shearer, P. M. (2009). A global view of the lithosphere-asthenosphere boundary. *Science*, *324*(5926), 495–498. https://doi.org/10.1126/science.1169754

Rychert, C. A., & Shearer, P. M. (2011). Imaging the lithosphere-asthenosphere boundary beneath the Pacific using ss waveform modeling. *Journal of Geophysical Research*, *116*(B7), B07307. https://doi.org/10.1029/2010jb008070

Rychert, C. A., Tharimena, S., Harmon, N., Wang, S., Constable, S., Kendall, J. M., et al. (2021). A dynamic lithosphere–asthenosphere boundary near the equatorial mid-atlantic ridge. *Earth and Planetary Science Letters*, *566*, 116949. https://doi.org/10.1016/j.epsl.2021.116949

Sacks, I., Snoke, J., & Husebye, E. (1979). Lithosphere thickness beneath the baltic shield. *Tectonophysics*, *56*(1–2), 101–110. https://doi.org/10.1016/0040-1951(79)90016-7

Schmerr, N. (2012). The gutenberg discontinuity: Melt at the lithosphere-asthenosphere boundary. *Science*, *335*(6075), 1480–1483. https://doi.org/10.1126/science.1215433

Schmerr, N., & Garnero, E. (2006). Investigation of upper mantle discontinuity structure beneath the central Pacific using ss precursors. *Journal of Geophysical Research*, *111*(B8), B08305. https://doi.org/10.1029/2005jb004197

Shearer, P. M. (1991). Constraints on upper mantle discontinuities from observations of long-period reflected and converted phases. *Journal of Geophysical Research*, *96*(B11), 18147–18182. https://doi.org/10.1029/91jb01592

Stern, T., Henrys, S. A., Okaya, D., Louie, J. N., Savage, M. K., Lamb, S., et al. (2015). A seismic reflection image for the base of a tectonic plate. *Nature*, *518*(7537), 85–88. https://doi.org/10.1038/nature14146

The MELT Seismic Team (1998). Imaging the deep seismic structure beneath a mid-ocean ridge: The melt experiment. *Science*, *280*(5367), 1215–1218. https://doi.org/10.1126/science.280.5367.1215

Tharimena, S., Rychert, C., Harmon, N., & White, P. (2017). Imaging Pacific lithosphere seismic discontinuities—Insights from ss precursor modeling. *Journal of Geophysical Research: Solid Earth*, *122*(3), 2131–2152. https://doi.org/10.1002/2016jb013526

Turcotte, D., & Oxburgh, E. (1967). Finite amplitude convective cells and continental drift. *Journal of Fluid Mechanics*, *28*(1), 29–42. https://doi.org/10.1017/s0022112067001880

Turcotte, D. L., & Schubert, G. (2002). *Geodynamics*. Cambridge university press.

USGS. (2017). *Preliminary determination of epicenters (PDE) bulletin: US geological Survey*. US Geological Survey Earthquake Hazards Program.

Vidale, J. E., & Benz, H. M. (1992). Upper-mantle seismic discontinuities and the thermal structure of subduction zones. *Nature*, *356*(6371), 678–683. https://doi.org/10.1038/356678a0

Wang, S., Constable, S., Rychert, C. A., & Harmon, N. (2020). A lithosphere-asthenosphere boundary and partial melt estimated using marine magnetotelluric data at the central middle atlantic ridge. *Geochemistry, Geophysics, Geosystems*, *21*(9), e2020GC009177. https://doi.org/10.1029/2020gc009177

Wessel, P., & Smith, W. H. F. (1995). New version of the generic mapping tools released. *Eos Transactions AGU*, *76*(33), 329. https://doi.org/10.1029/95eo00198

Xue, J., Zhou, Y., & Chen, Y. J. (2015). Tomographic resolution of plume anomalies in the lowermost mantle. *Geophysical Journal International*, *201*(2), 979–995. https://doi.org/10.1093/gji/ggv067

Yamauchi, H., & Takei, Y. (2016). Polycrystal anelasticity at near-solidus temperatures. *Journal of Geophysical Research: Solid Earth*, *121*(11), 7790–7820. https://doi.org/10.1002/2016jb013316

Zhou, Y. (2009). Multimode surface wave sensitivity kernels in radially anisotropic Earth media. *Geophysical Journal International*, *176*(3), 865–888. https://doi.org/10.1111/j.1365-246x.2008.04010.x

Zhou, Y., Dahlen, F., Nolet, G., & Laske, G. (2005). Finite-frequency effects in global surface-wave tomography. *Geophysical Journal International*, *163*(3), 1087–1111. https://doi.org/10.1111/j.1365-246x.2005.02780.x

Zhou, Y., Nolet, G., Dahlen, F. A., & Laske, G. (2006). Global upper-mantle structure from finite-frequency surface-wave tomography. *Journal of Geophysical Research*, *111*(B4), B04304. https://doi.org/10.1029/2005JB003677